J Intell Robot Syst (2009) 54:535–565
DOI 10.1007/s10846-008-9246-1

Multi-Scale Adaptive Sampling with Mobile Agents for Mapping of Forest Fires

Muhammad F. Mysorewala · Dan O. Popa · Frank L. Lewis

Received: 20 October 2007 / Accepted: 6 June 2008 / Published online: 27 August 2008

Abstract The use of robotics in distributed monitoring applications requires wireless sensors that are deployed efficiently. A very important aspect of sensor deployment includes positioning them for sampling at locations most likely to yield information about the spatio-temporal field of interest, for instance, the spread of a forest fire. In this paper, we use mobile robots (agents) that estimate the time-varying spread of wildfires using a distributed multi-scale adaptive sampling strategy. The proposed parametric sampling algorithm, "*EKF-NN-GAS*" is based on neural networks, the extended Kalman filter (EKF), and greedy heuristics. It combines measurements arriving at different times, taken at different scale lengths, such as from ground, airborne, and spaceborne observation platforms. One of the advantages of our algorithm is the ability to incorporate robot localization uncertainty in addition to sensor measurement and field parameter uncertainty into the same EKF model. We employ potential fields, generated naturally from the estimated fire field distribution, in order to generate fire-safe trajectories that could be used to rescue vehicles and personnel. The covariance of the EKF is used as a quantitative information measure for sampling locations most likely to yield optimal information about the sampled field distribution. Neural net training is used infrequently to generate initial low resolution estimates of the fire spread parameters. We present simulation and experimental results for reconstructing complex spatio-temporal forest fire fields "truth models", approximated by radial basis function (RBF) parameterizations. When compared to a conventional raster scan approach, our algorithm shows a significant reduction in the time necessary to map the fire field.

Keywords Adaptive sampling · Sensor fusion · Kalman filter · Potential fields · Environmental monitoring · Forest fires

M. F. Mysorewala (✉) · D. O. Popa · F. L. Lewis
Automation & Robotics Research Institute, The University of Texas,
Arlington, TX, USA
e-mail: muhammad@arri.uta.edu

1 Introduction

Wildfire is a major natural disturbance that has tremendous impact on the environment, humans and wildlife, ecosystem, weather, and our climate. There appears to be an increasing trend of natural fire activity. The 2006 wildland fire season set new records in both the number of reported fires as well as acres burned in the US, with a total of 96,385 fires and 9,873,429 acres burned. This season was 125% above the 10-year average (www.nifc.gov). During this time, fire suppression resources were in high demand and there was a critical need for air tankers, crews, and personnel. The fire suppression cost for 2006 was 1.5 billion dollars compared to 690 million dollars for 2005.

Fire management strategies have changed today with the introduction of new fire suppression tools. Use of advanced technology helps in fire mapping using satellite imagery, accurate weather forecasts, and fire behavior modeling. Airborne and spaceborne observation platforms, air-tankers, bulldozers, and tractor plows are commonly used for fire mapping and control, and they improve the safety of firefighters and the general public. Tractors are used for clearing vegetation and building fireline faster more efficiently than human firefighters. Rescue operations consist of searching for and removing trapped occupants in hazardous conditions. Although the use of advanced technology has reduced human involvement, self-preservation of the personnel manning the observation platforms remains a critical issue. One of the best ways to reduce the risk for firefighting personnel is to gather information about the spread of the fire in real time using autonomous robots; however, such technology has not yet been adopted.

However, it seems entirely plausible that in the near future, tracking and prediction of the spread of forest fires will be achieved by mobile robots equipped with sensors for measuring environmental conditions such as temperature, fire intensity, humidity, slope, wind strength and direction, etc. Fire spread and intensity information "measures" should then be used to reposition the robots in order to achieve optimal sampling of this spatio-temporal field, e.g. to describe its spread as accurately, and in the shortest time possible. It is common to use aerial and satellite photos, with different sensors to aid the fire modeling [5, 27], but the information is available at a very low-sampling rate (temporal-resolution problem) and also it is not very accurate (spatial and spectral resolution problem). To address these challenges, it is desirable to use a combination of (a) low-fidelity, high-altitude sampling using aerial satellite imaging and topographic mapping, and b) high-fidelity, low-altitude atmospheric sensing for fire intensity, air temperature, humidity, smoke, wind, etc., using mobile robotic vehicles. We call this strategy "multi-scale" sampling, in recognition of the fact that it covers multiple scales of magnitude in length and resolution [41].

Due to the time-critical nature of the fire mapping problem, simply requiring that the robots perform a raster scan or randomly sample the fire field would be sub-optimal because of stringent time and energy constraints. In the context of optimizing the sampling of spatio-temporal fields with mobile robots, several adaptive sampling (AS) algorithms have recently been proposed [4, 15, 31, 34, 41]. The term "adaptive" refers to choosing the sampling points based on the amount of information they provide about the spatio-temporal distribution that we wish to map. Examples of spatially distributed fields that can be monitored using adaptive sampling are salinity

in lakes [34], humidity in forests [41], and chemical leaks in buildings, as it is done in odor sampling [4, 17, 38], chemical plume tracing using under-water vehicles [8], and wide-area exploration [26].

A problem, which naturally arises in the process of sampling, is making sure that the measurements of sensors are correlated with their position, and that the data from multiple sensors is fused efficiently. Multiple vehicle localization and sensor fusion are by now classic problems in robotics, and there has been considerable progress in the two decades in these areas [10, 37]. Furthermore, distributed field variable estimation is relevant to charting and prediction in oceanography and meteorology, and has also received considerable attention [6]. In both contexts, measurement uncertainty can be addressed using Kalman filter estimation [1, 23]. Recently, Sanderson and Popa described a combined multi-agent AS problem coupling wireless sensor nodes with mobile robots, and using information measures to reposition the robots in order to achieve near-optimal sampling of a distributed field [33]. Unlike other non-parametric sampling methods [15, 41], this approach requires a parametric field description of the sampled field, and a dynamic model for robots.

In our previous work [30–32], we presented both simulation and experimental results for single- and multiple-agent adaptive sampling by combining localization and navigation of mobile robotic sensor nodes with sensor field estimation. We also compared the convergence properties of several sampling strategies such as standard AS, greedy AS and raster scanning for spatially distributed parametric fields. We showed that the heuristic greedy adaptive sampling (GAS) improved performance over traditional raster scanning for stationary fields. However, previous examples described sampling relatively simplistic fields, such as linear gradients, or fields with few Gaussian sources.

Forest fire mapping using robots is a typical example of a real-time density estimation problem, and has been covered in detail in [39, 40]. The distribution can be assumed parametric or non-parametric. Parametric and non-parametric distributions are considered in [3] for adaptive sampling of ocean using under-water vehicles. Non-parametric fields are accurate as they do not assume any functional form of distribution in advance. Examples of solutions with non-parametric distribution assumptions is the Occupancy Grid for discrete landmark mapping [7], which is an example of a solution involving exploration, instead of planned sampling missions. With no a priori information, the sampling problem becomes an exploration problem in the beginning, until enough samples are taken and distribution assumptions can be made. A solution for non-parametric ocean sampling is given in [15] where the adaptive sampling criteria take more samples in high-variance area and fewer samples in low-variance areas using a non-uniform size grid.

The physics of the fire behavior, its spread and immediate effects have been studied extensively [5, 9, 18, 36]. Fuel, weather, and topography are the key considerations in the spreading of fire. Most common are the semi-empirical fire modeling that uses Rothermel's equation for calculation of local rate of fire spread [9, 36], Huygen's principle for modeling the shape of fire front [9, 36] and the use of discrete-event cellular automata models [19, 24, 28, 42]. Furthermore, neural network and other classification schemes are being used for some time for supervised classification of remote sensing data, especially in applications of urban planning and atmospheric modeling, for instance, in order to classify the area as water, forest, wetlands, lakes,

etc [24]. Since the fire spread phenomena is too complex to understand, and the effect of each and every variable is difficult to predict, a neural network can be used as a "black box" for measuring the influence of the independent variables. For instance, representing the fire spread as a parametric time-varying sum of several Gaussians makes for an attractive approximation that we will make use of in this paper.

Complex forest fires distributions are obtained through the use of radial basis function (RBF) neural nets. If the Occupancy Grid scheme is used for sampling of this kind of continuous distribution, additional complex smoothing of certain regions will be required. Instead, we rely on the assumption of overlapping normal distributions, valid for all continuous fields based on the Universal Approximation Theorem [14]. RBF parametric models resulting from a low-resolution image, for instance, serve as good initial approximations for the fire field. When combined with a high-resolution adaptive sampling strategy, the errors introduced by low-resolution sampling and training are reduced. Sampling is done heuristically by mobile robots (agents) that search in the vicinity of the current location for future sampling locations minimizing field parameter uncertainty. This results in a quick, high-resolution reconstruction of the field at the end of the sampling process. Furthermore, the parametric description of the field can be used along with the robot dynamic model to reduce the localization uncertainty of the agents. This may not be needed in scenarios where global positioning system (GPS) measurements are available, but it is critical in GPS-denied environments, such as underwater or inside buildings.

In this paper, we test the validity and performance of our sampling algorithm in increasingly complex fire spread scenarios. First, we use a simple time-varying elliptical forest fire spread model that has been fitted to empirical data. This model considers a decreasing intensity Gaussian distribution from the head of fire to the fire tail. The model is accurate at the beginning of the fire spread, and less accurate as time goes on. In later sections of the paper we consider more realistic fire spread models simulated by cellular automata (CA), using discrete rules to decide the burning of certain cells based on conditions at neighboring cells. We approximate a low-resolution image of this field by a RBF neural network training algorithm that also acts as a classifier. The objective of the classification is to introduce more neurons in high-variance areas of the field, and fewer neurons in low-variance areas. Training of the neural net is only needed infrequently, and it need not be very accurate.

In addition to sampling and reconstruction of the fire field, it is sometimes necessary to direct the robots or human personnel through this field and avoid dangerous locations, e.g. "hot zones". This type of navigation can be accomplished using potential fields [11, 16], and the estimated fire field model itself can serve as the navigation potential. Extensive research has been done in the area of path planning using potential fields for robotic vehicles [22]. Obstacle avoidance or goal attainment schemes often use penalty functions to bend feasible paths around obstacles as it was introduced by Krogh [21] and Khatib [20]. As the fire intensity field is generated via sampling, we use it to generate fire-safe trajectories to and from rescue locations for firefighter human crews.

The sampling and navigation algorithms presented in this paper are validated using extensive, realistic, time-varying forest fire simulation models. Using a camera projector system and mobile wireless robotic nodes, ARRI-Bots [31, 32], the algorithms are also validated experimentally in a controlled lab environment.

Uncertainties in localization of the mobile robots are not considered here, but they can be easily incorporated into the EKF framework as described in our past work.

The paper is organized as follows: in Section 2 we present the formulation for EKF-based adaptive sampling algorithm for spatio-temporal distributions; in Section 3 we describe the two parametric models used to describe the spread of a forest fire; in Section 4 we discuss the parameterization of the field by interpreting remote-sensing images; in Section 5 we illustrate the multi-scale adaptive sampling algorithm on simulated fire spread models; in Section 6 we discuss potential fields-based path planning for robots navigating through the estimated fire field; in Section 7 we present simulation results that compare traditional raster scan sampling and an improved search heuristic, the Greedy Adaptive Sampling (GAS) method. We present sampling results for a simple elliptical field, a more complex stationary field, and finally a very complex, time-varying fire field. In Section 8 we discuss the experimental sampling results, and Section 9 presents the simulations results for potential field-based path planning. Finally, Section 10 concludes the paper.

2 EKF Adaptive Sampling of Spatio-Temporal Distributions Using Mobile Agents

In our previous work [31, 32, 34], we proposed a nonlinear EKF approach as an efficient framework for combining the uncertainty in robot localization with errors in field sensor measurements. We use a state-measurement minimization of the EKF covariance matrix norm to achieve effective adaptive sampling using a variety of mobile robotic platforms including underwater and in-door vehicles. Localization uncertainties are especially relevant in GPS-denied environments, but they can also be present in situations where local visual information is unavailable (for instance, due to thick smoke), and GPS data rates are slow. The past models we considered were time-stationary and simple, for instance, linear gradients, or one or two Gaussians. In this paper, we consider time-varying complex models stemming from realistic fire-spreading simulations. We integrate model parameter estimation for the field variable (fire temperature) with estimation of the uncertainty in the mobile robot localization and use the overall estimate covariance for sampling. Therefore, we can reduce localization uncertainty by building accurate models of distributed fields and vice versa. For instance, if a robot is sampling an unknown field, but its location is accurately known, a distributed parameter field model can be constructed by taking repeated field samples. Later on, this field model can be used to reduce the localization error of the robot.

The multi-agent AS problem considered in this paper can be described as follows:

Assumptions

1) We are describing a nonlinear spatio-temporal field variable via a parametric approximation $Z = Z(\boldsymbol{A}, \boldsymbol{X}, t)$ depending on an unknown parameter vector $\boldsymbol{A}$, position vector $\boldsymbol{X}$, and time t.
2) N robotic vehicles (agents) sample the field with localization and sensing uncertainty in order to obtain higher resolution estimates of the field, and to improve their own location estimates.

3) The number of field parameters (M) and their initial guess is based on a hypothesis originating from prior knowledge of the field, or from a low-resolution image of the entire field approximated via an RBF neural network.

We propose a GAS heuristic strategy to choose sampling locations for the mobile agents. GAS uses the EKF covariance matrix as the information measure:

GAS Heuristic: Determine future robot sampling locations $X^i_{k+1(1\le i\le N)}$, belonging to a neighborhood of the current locations $\vartheta\left(X^i_{k(1\le i\le N)}\right)$, chosen such that the estimated error covariance of the aggregate (robot-field) nonlinear EKF is minimized.

We describe the state transition and measurement equations during sampling through nonlinear mappings (functions h, m, f, and g) as follows:

– Robot state dynamics:

$$X^i_{k+1} = X^i_{k+1} + h\left(X^i_k, U^i_{1k}\right) + w^i_k, \tag{1}$$

where X^i_k, U^i_k are the ith vehicle state and control input, where the state has noise covariance matrix is $E\left[w^i_k\left(w^i_k\right)^T\right] = Q^i_{1k}$.

– Field parameter dynamics:

$$A_{k+1} = A_k + m\left(A_k, U_{2k}\right) + \alpha_k\ , \tag{2}$$

where $\boldsymbol{A}_k$ is a vector of unknown coefficients describing the field with noise covariance matrix $E\left[\alpha_k\alpha_k^T\right] = Q_{2k}$, and $\boldsymbol{U}_{2k}$ is the uncontrollable (but measurable) "field evolution vector". This parameter is a slow-varying correction factor in the field parameters, assuming that infrequent, low resolution measurements of the entire field are available.

– Robot position output:

$$Y^i_k = f\left(X^i_k\right) + \xi^i_k\,, \tag{3}$$

where the output noise covariance is $E\left[\xi^i_k\left(\xi^i_k\right)^T\right] = R^i_{1k}$.

– Distributed field variable measurement model:

$$Z_k = g\left(X^i_k, A_k\right) + \nu_k\ , \tag{4}$$

where Z_k is the field variable with measurement noise covariance $E\left[\nu_k\nu_k^T\right] = R_{2k}$.

– Field evolution factor measurement:

$$\tilde{U}_{2k} = U_{2k} + \beta_k\ , \tag{5}$$

with measurement noise covariance is $E\left[\beta_k\beta_k^T\right] = R_{3k}$.

In [31] and [32], we presented different cases of the above general formulation. One combined the location states estimates X^i_k and field parameter estimates A_k in a joint-EKF, and used the combined uncertainty of the states as our information measure. Another fused output measurements Y_k and Z_k, and considered the impact of dead-reckoning localization of the robots. We also considered the two cases when both sensor node position measurement Y_k and field variable measurement Z_k

are available, and when only Z_k is available to estimate field parameters A_k and states X_k^i.

In this paper, we use the algorithm to map a complex forest fire field, which is time-varying, using measurements performed at different rates and length scales. For slow-varying fields, the time update is performed at a slower rate compared to the measurement update. We assume that the time update (Eq. 2) is performed at a sampling rate of T_d by high-spatial infrared imaging an uncertainty represented by the process covariance noise Q_{Td}. The field evolution is measured by the difference $\left(\tilde{U}_{Td+1} - \tilde{U}_{Td}\right)$ between these consecutive measurements. High rate field measurement updates are then done via robotic sampling, with uncertainty represented by covariance noise R_{2k}.

Assuming that the ith robot location Y_k^i is measured using absolute localization (such as via GPS), we can ignore the dynamics of robots and we simplify the state and output equations as:

$$\begin{aligned} A_{k+1} &= A_k + (U_{Td+1} - U_{Td}) + \alpha_{Td+1} \\ \tilde{U}_{Td+1} &= U_{Td+1} \\ Y_k^i &= X_k^i \\ Z_k &= g\left(Y_k^i, A_k\right) + \nu_k \end{aligned} \tag{6}$$

Therefore, the EKF equations become:

$$\begin{aligned} P_{k+1}^- &= P_k + Q_{Td+1},\ \hat{A}_{k+1}^- = \hat{A}_k + \left(\tilde{U}_{Td+1} - \tilde{U}_{Td}\right) \\ H_k &= \frac{\partial g_k}{\partial\left(Y_k^i, \hat{A}_k^-\right)} \\ P_{k+1} &= \left(\left(P_{k+1}^-\right)^{-1} + H_{k+1}^T R_{k+1}^{-1} H_{k+1}\right)^{-1} \\ \hat{A}_{k+1} &= \hat{A}_{k+1}^- + P_{k+1} H_{k+1}^T R_{k+1}^{-1}\left[Z_{k+1} - g_{k+1}\left(Y_{k+1}^i, \hat{A}_{k+1}^-\right)\right] \end{aligned} \tag{7}$$

where, $Q_k = Q_{Td+1}$, $R_k = R_{2k}$.

The GAS algorithm then moves the robotic vehicle from X_k^i to X_{k+1}^i such that the following p-norm of the covariance matrix is minimized over the vehicle neighborhood $\vartheta\left(X_k^i\right)$:

$$m\left(X_k^i, A_k\right) = \|P_k\|_p, m\left(X_{k+1}^i, A_{k+1}\right) \leq m\left(X_k^i, A_k\right),\ \forall X^i \in \vartheta\left(X_k^i\right). \tag{8}$$

3 Parametric Description of Forest Fire Spread

The fire-spreading phenomenon is highly complex, and existing mathematical models of its spread require extensive computing resources. Regenerating time-varying fire spread models might be adequate to run in batch mode, but they are difficult to use in real-time fire-fighting scenarios. However, these models help in understanding the influence of different factors on fire propagation without the need for an analytical solution. Existing fire spread models are divided into three classes: empirical, semi-empirical and physical models. Several powerful software applications such

as FARSITE, FireGIS, Fire!, SPREAD, etc. are available to simulate the fire spread [9].

Many factors influence fire behavior, with fuels, weather and topography being the primary factors [1, 12, 13, 36, 43]. Parametric models have been empirically fitted to observe data using four primary inputs: fuel type, fuel moisture, wind and slope. Second-order variables such as temperature, humidity, shading and shelter operate through one of the four primary inputs. The effect of the primary inputs is described below:

Slope	Fire can spread significantly faster up a slope than on level terrain in the same fuels. In many cases, topographic maps are very helpful for understanding the fire spread.
Wind	Wind speed and direction are the most critical factors required for predicting fire behavior.
Fuel	Fuel types are lumped together into different models. Fuel loading, fuel depth, fuel particle density, head content of fuel, moisture of extinction, and surface area-to-volume ratio are the factors used to further describe it.
Fuel moisture	Fuel moisture is an expression of the amount of water in the fuel component. It determines both fire intensity and the heat required to bring the fuel ahead of spreading fire up to the ignition temperature.

3.1 Simple Elliptical Fire Spread Model

Given homogeneous fuel and weather conditions, and assuming a constant, moderate wind, a fire growing from an ignition point is initially close to an elliptical shape. Strong winds or steep slopes can elongate the shape, but it remains consistent until fuels or wind change. The spread distance is the product of projection time and the rate of spread.

The most common simulation model for forest fires growth from point sources is using the Huygens principle [36], which considers the elliptical nature of fire growth with (a,b) as the minor and major axes, respectively, and c as the distance from center of ellipse to the fire source (x_s, y_s). Figures 1 and 2 show the elliptical spread of a fire starting at an ignition point. Since this function is a constrained Gaussian, it will later be used as a RBF function with constraints. For a typical case, the dimensions of the elliptical axis can be calculated by the following equations:

$$
\begin{aligned}
& a = 0.5\frac{R + R/HB}{LB}, b = \frac{R + R/HB}{2}, c = b - R/HB \\
& LB = 0.936.e^{0.2566U} + 0.461.e^{-0.1548U} - 0.937 \\
& HB = \frac{LB + (LB^2 - 1)^{0.5}}{LB - (LB^2 - 1)^{0.5}}
\end{aligned} \tag{9}
$$

where R is the fire spread rate in foot per minute, LB is the length to breadth ratio, HB is the head-to-back ratio, and U is the wind speed.

The variable which we wish to map in space and time is a constrained Gaussian distribution of temperature. We further assume that the maximum fire temperature I, variance σ and y_0 are time invariant, while the firehead ($x_0(t)$, $y_0(t)$) location is

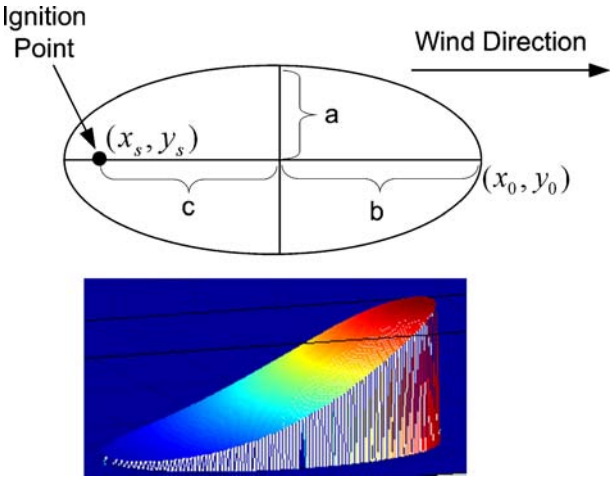

Fig. 1 Elliptical fire growth model represented by an elliptically constrained RBF function

proportional to the fire spread rate, which in turn is proportional to the wind speed. If $y_0(t) = C$ (e.g. fire spreads horizontally), then the fire intensity is given by:

$$g(X, A, t) = \begin{cases} I \exp\left[-\dfrac{(x - x_0(t))^2 + (y - y_0)^2}{2\sigma^2} \right], & \dfrac{(x - x_0(t) + b(t))^2}{b(t)^2} + \dfrac{(y - y_0)^2}{a(t)^2} \le 1 \\ 0 & otherwise \end{cases}, \tag{10}$$

where, $x_0(t) = x_s + b(t) + c(t)$.

If wind is blowing at an angle ϕ to the x-axis, the new parametric equation of ellipse can be derived by a rotation around the fire source (x_s, y_s) by angle ϕ. In this case, Eq. 10 becomes:

$$g(X_{\text{new}}, A, t) = I \exp\left[-\frac{\|X_{\text{new}} - X_s\|^2 + \|X_s - X_0\|^2 + 2(X_{\text{new}} - X_s)^T R_\phi (X_s - X_0)}{2\sigma^2} \right], \tag{11}$$

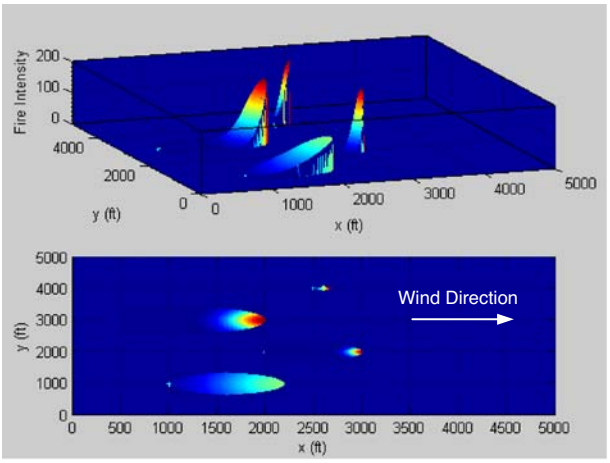

Fig. 2 Four fire ellipses originated at different points and with different spread rate, peak intensity and variance. The head of fire is the mean of the Gaussian distribution

where R_ϕ^T is a 2×2 rotation matrix by angle ϕ, and $X_{\text{new}} = \begin{bmatrix} x_{\text{new}} & y_{\text{new}} \end{bmatrix}$, $X_o = \begin{bmatrix} x_o & y_o \end{bmatrix}$, $X_{\text{s}} = \begin{bmatrix} x_{\text{s}} & y_{\text{s}} \end{bmatrix}$.

3.2 Complex Cellular Automata (CA)-based Discrete Event Model

The Huygens fire spread model is quite simple, but it is quite reasonable for short intervals of time after ignition. Because it assumes uniform, continuous fuel, uniform wind velocity throughout the burning area and flat terrain, the model becomes inaccurate if the fire spreads over large distances. Cellular automata (CA) are very good for modeling and simulating complex dynamical systems whose evolution depends on the state of the current cell, neighboring cells, wind, slope, and fuel. This scheme can also recover the Huygens fire spread model discussed in a previous section at a cellular level. The fire spread region is divided into cells, as shown in Fig. 3a, and the fire propagates from cell to cell governed by discrete-event rules, which iterate the temperature at the next sample time as a function of the temperature of its cell neighbors, and of several local fire parameters. The transition rules can be written as:

$$T_{i,j}^{k+1} = f\left(T_{i,j}^{k}, T_{i,j,1}^{k}, ..., T_{i,j,4}^{k}, \text{wind}, \text{slope}, \text{fuel}\right). \tag{12}$$

Each cell is considered to be in one of the following four states (*inactive*, *unburned*, *burning* and *burned*) as shown in Fig. 3b [18]. The fire starts from a hotspot in an elliptical shape in the sense that each burning cell generates an ellipse with focus on the cell center. Depending on fuel type, moisture, slope, wind, and the state of the surrounding cells, each may have a different rate of increase of temperature (α), maximum temperature ($T_{\max}$), ignition temperature (T_{ignition}), rate of temperature decay (β), time threshold for switching to unburned state (t_{thresh}), and ignition time (t_{ignition}).

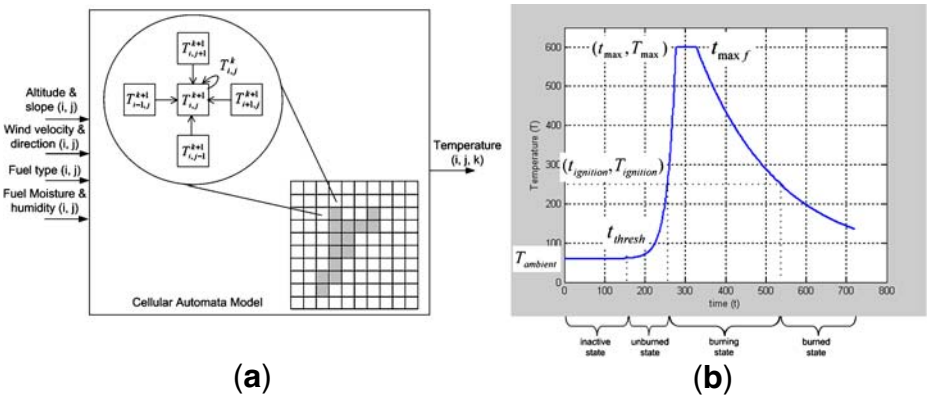

Fig. 3 CA model inputs–outputs (**a**), and temperature variation with respect to time (**b**)

The following set of equations governs the temperature variation with respect to time:

$$T(t) = \begin{cases} T_a & ; \ t \le t_{thresh} \\ T_a + e^{(t-t_{th})\alpha} & ; \ t_{thresh} < t \le t_{\max} \\ T_{\max} & ; \ t_{\max} < t \le t_{\max f} \\ T_a + (T_{\max} - T_a).e^{(t_{\max f}-t)\beta} & ; \ t > t_{\max f} \end{cases} \tag{13}$$

Qualitatively, the rules can be simply described as:

- A cell remains in *inactive* state while it is outside the *burning* ellipse. This situation corresponds to the case when none of its neighboring cells is in *burning* state. The state switches to *unburned* state when one of its neighbors starts *burning*.
- Once the cell switches from *inactive* state to *unburned* state, its temperature starts to rise at a rate of α, which depends on the fuel availability, wind, and terrain.
- The cell starts *burning* after it reaches the ignition temperature. The combustion duration and rate of temperature decay β depends on fuel, wind, and terrain.

Figure 4a, b shows a fire generated from the hot spot at (244,127) using CA at time instants $t = 2$ and 5. Initially, the fire spreads uniformly because the difference in the state of the cells is not significant. Also the fire shape is circular because slope

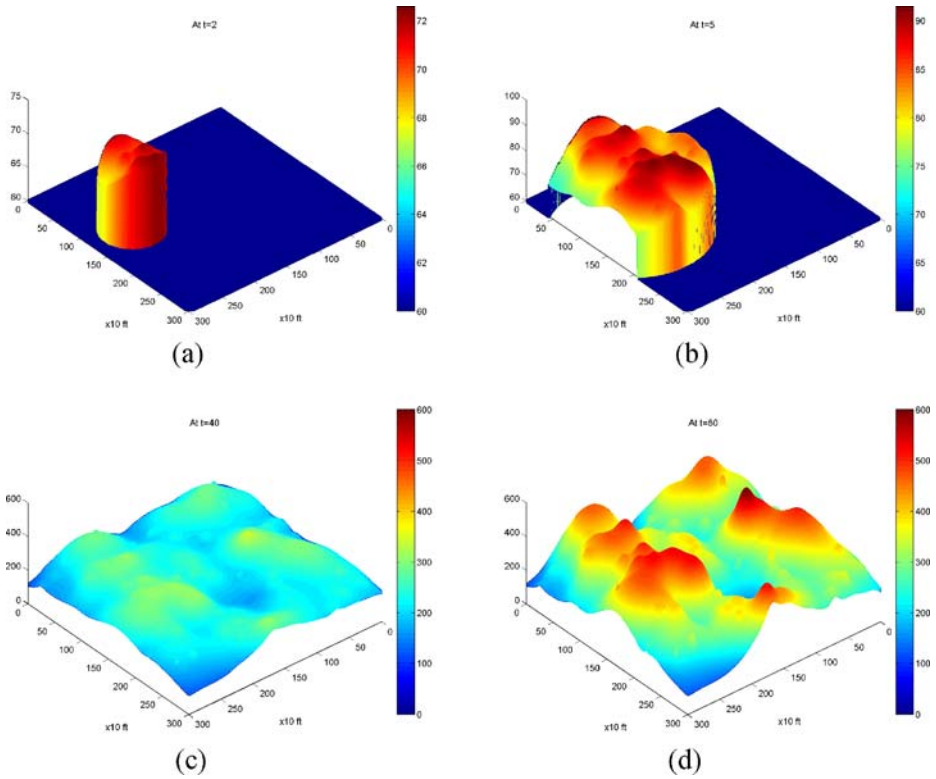

Fig. 4 2D fire spread using CA at time $t = 2$, 5, 40 and 80

variation and wind direction are not considered. But after some time the fire start to spread more wildly because of the difference in the fuel available in different cells. Figure 4c, d shows the fire at time $t = 40$ and 80 after most of the area with significant fuel content is burning.

The fire spread models presented in this section are not used to predict the spread of fire; rather, they are used as "truth models" in order to test our sampling algorithms. It will be through the use of direct sampling using robots that accurate spatio-temporal tracking of fires is accomplished.

4 Neural Network Parameterization of Fire Phenomena

Digital remote sensing images of forests can be acquired from field-based, airborne, and satellite platforms. Imagery from each platform can provide a data set with which forest analysis and modeling can be performed. Airborne images typically offer greatly enhanced spatial and spectral resolution over satellite images. In addition, airborne images provide greater control over capturing images from specific areas of interest and at different altitudes [5]. In this section, we discuss the parameterization of the fire spread model using a RBF neural net. We assume that low-resolution images are available from overhead observation platforms at infrequent time intervals.

4.1 RBF Neural Network System Parameterization of Fire Spread

In the case of fire distribution, an exact nonlinear model description is unattainable due to the high level of complexity. In order to obtain an initial approximation of the field, we train a neural network with a low-resolution "fire field image". Training is done once, at the beginning of the EKF estimation process (e.g., of sampling with robots), and the result is used as an initial hypothesis about the field distribution. The network is presented with training pairs, which in our case is the temperature at different locations taken from a low-resolution infrared image. The idea is to roughly approximate the complex spatio-temporal field with a sum-of-Gaussian parametric field by means of the Universal Approximation Theorem. Using the training algorithm, the network adjusts its weights so that the error between the actual and desired response is minimized, usually done by a least squares optimization criteria. Gaussian RBF approximation of a fire field is a good choice because, as we saw in Section 3.1, fire spread can be modeled as a constrained Gaussian at least for some period of time after ignition.

For simulation purposes, in Section 7 we will use a radial bases neural network using "*newrb*" available in Neural Network toolbox of MATLAB. "*newrb*" creates a two-layer network, with the first layer having *radbas* neurons and the second with *purelin* neurons. Both layers have biases, and the output of the network is simply:

$$g = \sum_{i=0}^{N} w_i \Phi_i \left(\| (X_i - c_i)\, s_i \| \right)$$

$$\Phi_i = \exp\left(- \| (X_i - c_i)\, s_i \| \right) = \exp\left\{ -s_i \sum_{j=1}^{P} \left(X_j - c_{ij} \right)^2 \right\}, \tag{14}$$

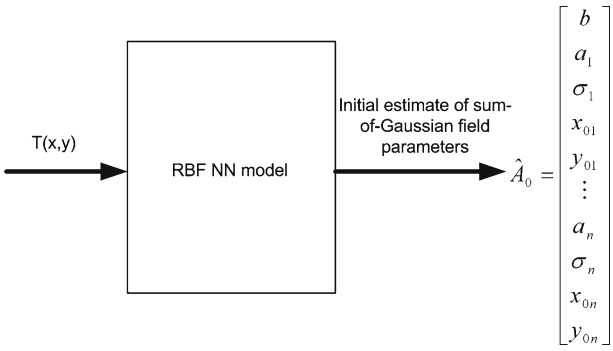

Fig. 5 Block diagram for inverse modeling. Parameters are estimated when inputs of NN are locations (x, y) and output is temperature

where X is the field location, $X \in \Re^P$. We wish to learn parameters w_0, w_1,...,w_N, centers c_1, c_2,..., c_N and the spread parameter s_1, s_2,...,s_N of the network. The spread parameters are the measure of the variance of the Gaussians. The hidden and output layer of the RBF network is optimized separately by a hybrid algorithm, e.g. the "self-organized selection of centers" [14]. A hybrid algorithm is necessary because the hidden layer evolve slowly compared to the linear layer. This algorithm uses k-mean clustering for the hidden layer and LMS algorithm for the output layer. This hybrid algorithm takes less time to train the neural network compared to backpropagation [25]. The learning algorithm requires setting a spread parameter. The larger spread is, the smoother the function approximation. Too large a spread means a lot of neurons are required to fit a fast-changing function. Too small a spread means many neurons are required to fit a smooth function. So the accuracy of the initial estimated field depends on image resolution, number of neurons, and the assumed spread factor. As shown in Fig. 5, temperature data from a low-resolution infrared image is used for training the RBF neural network, which gives an initial estimate of weights in linear layer, non-linear layer, and the center of Gaussians. These initial estimates are later used as initial conditions for the parameterized EKF-based sampling algorithm.

5 Simultaneous Sampling and Navigation for Mapping of Fire Fields

In this section, we combine the GAS algorithm with approximations of the field. To illustrate the approach, we first use the simple fire spread model from Section 3.1. Then, as a more general approach, we use the RBF parameter vector to represent the evolution in time of the field.

5.1 Elliptically Constrained Single Gaussian Time-Varying Fields

Here we assume that the fire is represented by a time-varying field in which model dynamic inputs U_{2k} depend on the measured velocity of spread (wind velocity). The Kalman filter equations are set up to estimate the peak intensity, variance, and mean

of the time-varying forest fire field. Using Eq. 2, we can write the fire model equation as:

$$A_{k+1} = A_k + B_{2k}U_{2k} + \alpha_k$$

$$\begin{bmatrix} I \\ \sigma \\ x_0 \\ y_0 \end{bmatrix}_{k+1} = \begin{bmatrix} I \\ \sigma \\ x_0 \\ y_0 \end{bmatrix}_k + \begin{bmatrix} 0 \\ 0 \\ r_{k+1}\Delta t_{k+1} \\ 0 \end{bmatrix} + \begin{bmatrix} 0 \\ 0 \\ \alpha \\ 0 \end{bmatrix}$$

$$\alpha \sim N(0, Q_2), \tag{15}$$

where Δt_{k+1} is the time from sample k to $k+1$, (x_0, y_0) is the location of head-of-fire where x_0 is a continuous function which is sampled at time $t_0, t_1, \ldots t_{k+1}$, r is a time-varying function describing the velocity of spread, r_{k+1} is the velocity of spread r for $(k+1)$ th sample.

The field parameter estimates are updated using Eq. 15. The measurement equations are given by Eq. 4 with noise covariance $v \sim N(0, R_2)$ The time and measurement update equations become:

Propagation:

$$\begin{aligned} \hat{I}^-_{k+1} &= \hat{I}_k, \hat{\sigma}^-_{k+1} = \hat{\sigma}_k, \left(\hat{y}_0\right)^-_{k+1} = \left(\hat{y}_0\right)_k \\ \left(\hat{x}_0\right)^-_{k+1} &= \left(\hat{x}_0\right)_k + r_{k+1}\Delta t_{k+1} \\ P^-_{k+1} &= P_k + Q_{k+1} \end{aligned} \tag{16}$$

Update:

$$\begin{aligned} \hat{H}_{k+1} &= \frac{\partial \hat{g}_{k+1}}{\partial\left(\hat{A}^-_{k+1}\right)} = \left[\frac{\partial g}{\partial \hat{I}^-_0}\frac{\partial g}{\partial \hat{\sigma}^-}\frac{\partial g}{\partial \hat{x}^-_0}\frac{\partial g}{\partial \hat{y}^-_0}\right]_{k+1} = \\ &= C\Bigg[1\hat{I}^-_{k+1}\left(\hat{\sigma}^-_{k+1}\right)^3\left\{\left(x_{k+1} - \hat{x}^-_{0k+1}\right)^2 + \left(y_{k+1} - \hat{y}^-_{0k+1}\right)^2\right\} \\ &\quad \times \frac{\hat{I}^-_{k+1}\left(x_{k+1} - \hat{x}^-_{0k+1}\right)}{\left(\hat{\sigma}^-_{k+1}\right)^2}\ \frac{\hat{I}^-_{k+1}\left(y_{k+1} - \hat{y}^-_{0k+1}\right)}{\left(\hat{\sigma}^-_{k+1}\right)^2}\Bigg], \end{aligned}$$

where $C = \exp\left[-\dfrac{\left(x_{k+1} - \hat{x}^-_{0k+1}\right)^2 + \left(y_{k+1} - \hat{y}^-_{0k+1}\right)^2}{2\left(\hat{\sigma}^-_{k+1}\right)^2}\right]$,

$$\begin{aligned} K_{k+1} &= P^-_{k+1}\widehat{H}^T_{k+1}\left(\widehat{H}_{k+1}P^-_{k+1}\widehat{H}^T_{k+1} + R_{k+1}\right)^{-1}, \\ P_{k+1} &= \left(I_{12} - K_{k+1}\widehat{H}_{k+1}\right)P^-_{k+1}, \\ \hat{A}_{k+1} &= \hat{A}^-_{k+1} + K_{k+1}\left\{\tilde{z}_{k+1} - \hat{g}_{k+1}\right\} \\ &= \hat{A}^-_{k+1} + K_{k+1}\left\{\tilde{z}_{k+1} - \hat{I}^-_{k+1}\exp\left[-\frac{\left(x_{k+1} - \hat{x}^-_{0k+1}\right)^2 + \left(y_{k+1} - \hat{y}^-_{0k+1}\right)^2}{2\left(\hat{\sigma}^-_{k+1}\right)^2}\right]\right\}. \end{aligned} \tag{17}$$

5.2 Formulation for Time-Varying Field Parameterized using RBF-NN

Let us consider now the more complex representation of the fire field model as generated by the CA model in Section 3.2. The proposed multi-scale sampling algorithm is outlined as follows:

Algorithm EKF-NN-GAS (multi-scale, multi-rate adaptive sampling)

- Step 1 (Setup): Give the environmental parameters and rules for fire spread as input to the CA model as shown in Fig. 7. This will generate a 2-D temperature field $T(x, y, t)$, which has a dimension of $m \times m$ at time t. In practice, this step is omitted, and replaced by the actual spread of the fire. Go to step 2.
- Step 2 (Initialization): Divide the field into square size grid of $n \times n$ cells, $n < m$ and average values in each cell. This provides a low-resolution version of the actual field of size $m/n \times m/n$, illustrated in Fig. 6. In practice, this low-resolution temperature distribution is acquired by an infrared image taken from an airborne platform. Go to step 3.
- Step 3 (Training): Train the RBF neural network using this low-resolution temperature data. In the training algorithm number of neurons and smoothness factor are specified. The number of neurons depends on the complexity of the field so that the error is minimized within an acceptable threshold. This gives the parameterized version of the field with N neurons and each neuron has parameters a, σ, x_0 and y_0 representing this RBF field. The error in the actual field and the initial estimate using neural network also gives a guess for initial error covariance P in later EKF steps. Go to step 4.
- Step 4 (High rate sampling): Spot measurement robots sample locations in a grid of size $p \times p$, (where $p \leq n < m$) based on a Greedy Adaptive Sampling criterion to minimize the error covariance. The EKF framework shown in Fig. 7 is used to correct the estimates as the subsequent measurements are available one by one. The robots location is calculated by GPS measurement, via dead-reckoning, or relative position measurements. Localization uncertainty is ignored in the simulation results of this paper, but should be considered along

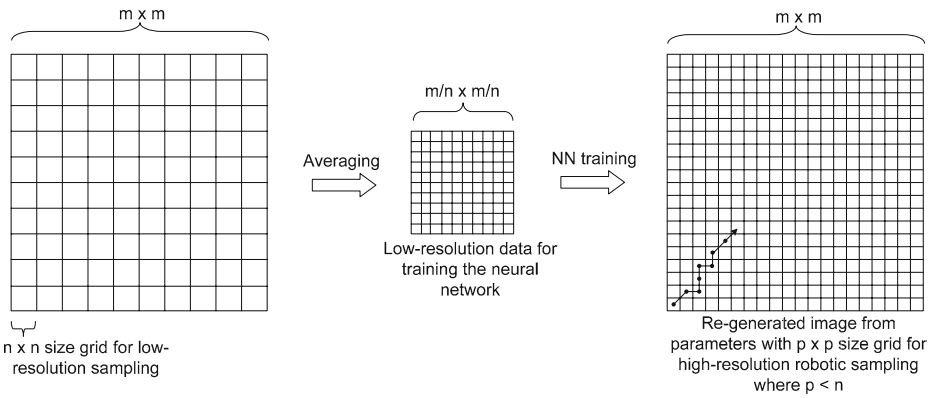

Fig. 6 Change in spatial resolutions for multi-scale sampling

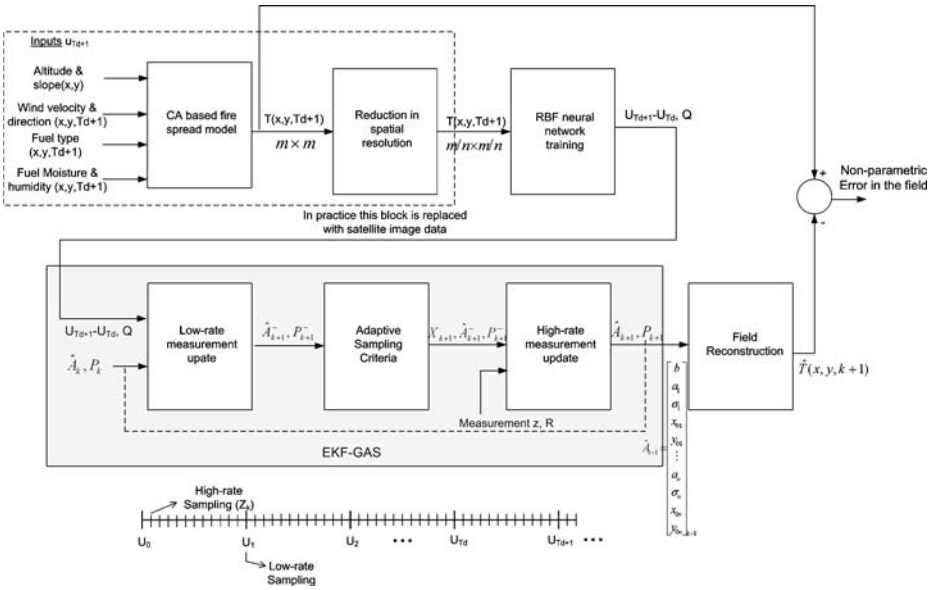

Fig. 7 Block diagram for temporal field model identification and parameter estimation, EKF-NN-GAS

with the robot dynamical model. The EKF sampling rate, T, should be as fast as sensory measurements from robots are available. Repeat Step 4 until new low-resolution updates of the entire field are available; otherwise, go to step 5.

– Step 5 (Low-rate sampling): Because of the time varying nature of the field, a low-resolution update of the field performed at a sampling rate T_d, and the evolution of the parameters is updated by comparing the low-resolution field distribution at time T_{d+1} and T_d. This involves repeating step 3 by retraining the neural network at time T_{d+1}, and updating the parameters since the last training at time T_d. The low-rate parameter update $\left(\tilde{U}_{Td+1} - \tilde{U}_{Td}\right)$ and its uncertainty Q is given as input to the EKF block for high-rate sampling update as shown in Fig. 7. Low-rate sampling is done at a very low rate approximately every 5 min compared to high-rate sampling, which takes several sensor measurements every minute. This scheme gives a better estimate of the time-varying field than if it was not included in the parameter time update. Go to step 4.

Since we ignore the sampling robot dynamics, the parameter estimation model is simply:

$$A_{k+1} = A_k + \alpha_k = \begin{bmatrix} b & a_1 & \sigma_1 & x_{01} & y_{01} & \cdots & a_N & \sigma_N & x_{0N} & y_{0N} \end{bmatrix}_k^T + \alpha,$$
$$\alpha \sim N(0, Q). \tag{18}$$

Moreover, if the field is time-varying, the field parameters propagate as:

$$A_{k+1} = A_k + \left(\tilde{U}_{Td+1} - \tilde{U}_{Td}\right) + \alpha\,, \tag{19}$$

where A_{k+1} is the field parameters update when $(k+1)^{th}$ sample is taken (step 4) and $\left(\tilde{U}_{Td}+1-\tilde{U}_{Td}\right)$ is the field parameters propagation obtained by performing step 5. The measurement model is:

$$Z_k = h\left(A_k\right)+\nu_k = b+\sum_{i=1}^{N} a_i \exp\left[-\sigma_i\left\{(x_k-x_{0i})^2+(y_k-y_{0i})^2\right\}\right]+\nu,$$
$$\nu \sim N\left(0,\, R\right). \tag{20}$$

The low-rate sampling update equations are now given by:

$$\hat{A}^{-}_{k+1} = \hat{A}_k + \left(\tilde{U}_{Td+1}-\tilde{U}_{Td}\right),$$
$$P^{-}_{k+1} = P_k + Q. \tag{21}$$

Step 5 does not reset the previous estimates but calculates the evolution of parameters $\left(\tilde{U}_{Td+1}-\tilde{U}_{Td}\right)$ based on current and past image, which is then added to the old parameter estimate $\hat{A}_k$ to get a prediction for a new estimate $\hat{A}^{-}_{k+1}$. Finally, equations similar to Eq. 17 can be used in the EKF sampling update. Figure 7 shows a block diagram of algorithm *EKF-NN-GAS*.

6 Potential Field to Aid Navigation Through Fire Field

The estimated fire field intensity distribution can be used as a repulsive potential to keep the fire fighters away from dangerous areas in the field and show them safe paths toward important destinations. Potential field methods create a vector field representing a navigational path based on a potential function. We use the sampled field variable intensity in order to plan collision-free paths around the fire "obstacles". Given a scalar potential function $U(X)$ where $X=(x,\, y)$, which depends on the rescuer position and the field intensity at that point, one can calculate forces governing the rescuer motion based on the gradient of the scalar potential field, similar to [22]:

$$\vec{F}\left(X\right) = -\vec{\nabla}U\left(X\right). \tag{22}$$

To plan paths, we consider the following forces (Fig. 8):

– Attractive forces toward goals:

$$\vec{F}_{att}\left(X\right) = -\vec{\nabla}U_{att}\left(X\right) = -\xi\rho_{goal}\left(X\right).\vec{\nabla}\rho_{goal}\left(X\right) = \xi\left(X-X_{goal}\right), \tag{23}$$

and

– Repulsive forces from obstacles which are fire ellipses:

$$U_{rep}\left(X\right) = \sum_{k=1}^{n} U_k\left(X\right),\quad U_k\left(X\right) = \lambda\frac{I_k}{\rho_k\left(X\right)^2},$$
$$\vec{F}_{rep}\left(X\right) = \sum_{k=1}^{n} \vec{F}_k\left(X\right),\quad \vec{F}_k\left(X\right) = -\vec{\nabla}U_k\left(X\right). \tag{24}$$

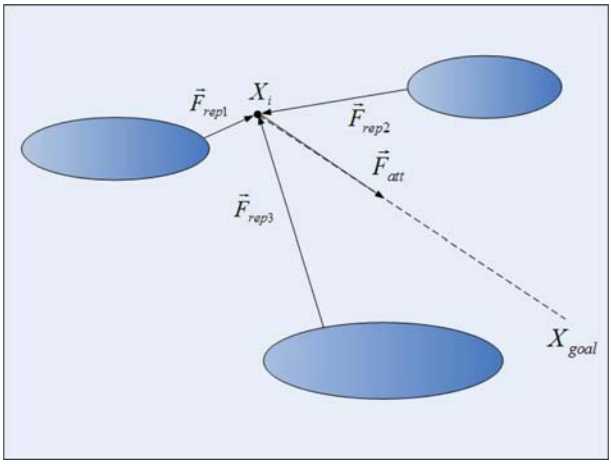

Fig. 8 The attractive forces on point X_i toward the goal X_{goal} and repulsive forces from the obstacles

where λ is the positive scaling factor, $\rho(X)$ is the Euclidean distance from X to the center of ellipse, r is the number of elliptical components close to current location and I_k is the fire intensity at the point on ellipse at the shortest distance from X. The trajectory is then updated using a depth-first planning algorithm, which constructs a path as the product of successive segments starting at the initial configuration X_i:

$$\vec{X}_{i+1} = \vec{X}_i + \delta_i \vec{F}_p, \tag{25}$$

where X_i and X_{i+1} are the origin and end extremities of the ith segment in the path.

7 Simulation Results

In this section, we use increasingly realistic fire spread models to validate the effectiveness of the sampling algorithm presented in Section 5.2 by comparing it to a basic raster scanning sampling approach. We also investigate the performance of the multi-rate EKF scheme to estimate the time-varying fire field model. First, we present sampling results on a single Huygens spread model. We then consider the case of a more complex but slow spreading fire field, and finally, we consider the case of the time-varying CA fire spread model. In all simulations, sampling is performed with a single robotic vehicle, and we are focusing on the accuracy of field estimation, rather than localization. For multiple vehicles, the EKF computations can be distributed among N robots as discussed at the end of this section.

7.1 Elliptically Constrained Single Gaussian Time-Varying Field

Simulations are performed to estimate four fire field parameters given in Eq. 11 for a single ellipse. It is assumed that there is a forest area of one square mile in which multiple robots take intensity measurement (or some measure of temperature) and estimates the desired parameters. The location of firehead x_0 is time varying.

The fire can spread at any arbitrary rate. In our simulation, we consider the case of a slow sinusoidal fire spread rate:

$$\dot{r} = \frac{2\pi}{60} \cos\left(\frac{2\pi}{60} t\right) \quad . \tag{26}$$

The rate equation in Eq. 26 is an arbitrary example. Other choices will not affect the rate of convergence as long as the spread model is known and the rate of spread is much smaller than the speed of sampling. Here, the increase in x_0 is sinusoidal with respect to time and space as shown in Fig. 9, and the other parameters are stationary. A comparison is done between sampling using raster scanning and heuristic greedy approach. The GAS algorithm looks for the next best sampling location in a circle of 50-ft radius around the currently sampled location, which gives the maximum information on the field parameters, as shown in Fig. 9. Raster scanning does a row-by-row scanning.

Table 1 shows a comparison of GAS and raster Scanning when sampling is performed for 60 min. It is assumed that robot's navigation speed is 30 ft/min. Here we ignore the robot sampling and processing time, while $Q = 0$, $R_1 = 0.1$.

Results indicate that GAS approach has faster convergence and require a considerably less number of sampling points. In Table 1, the norm of error covariance P_k is 7.3 for GAS and 44.2 for raster scanning after 60 min of sampling. If we continue our sampling, raster scanning takes almost six times more time than GAS to converge to the same estimate value (Fig. 10). It is also observed that error covariance decreases very slowly for raster scanning and it actually takes almost the entire sampling area to reduce the uncertainty to converge the estimates close to actual values. Raster scanning shows worst results when row-by-row scanning is being done in an area where the parameter of interest does not vary significantly.

7.2 Simple RBF Stationary Field

In Fig. 11a, we show a simple case where a Sum-of-Five-Gaussians field is approximated by a RBF neural network with five neurons. A low-resolution version of

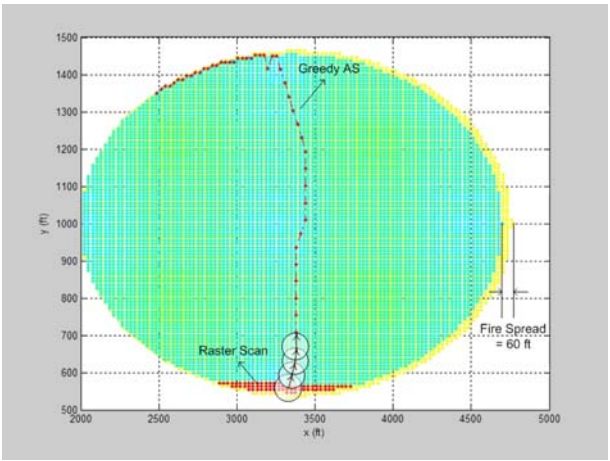

Fig. 9 Greedy Adaptive Sampling algorithm that looks for the appropriate location on the elliptical fire field to sample in a circle of radius 'r'. The location that gives maximum information about the field parameters is sampled. It also shows the row-by-row Raster scanning and the fire spread

Table 1 Comparison of raster scan and greedy AS

		A_0	A_k	$\hat{A}_0$	$\hat{A}_k$	P_0	P_k
Greedy AS ($k = 49$)	I	80	80	90	79.4	10	0.7
	σ	400	400	410	401.1	20	4.9
	x_0	2,700	2,760	2,720	2,759.7	50	3.8
	y_0	1,000	1,000	1,020	1,001.2	50	3.8
Raster Scan ($k = 68$)	I	80	80	90	85.7	10	2.4
	σ	400	400	410	397.9	20	5.1
	x_0	2,700	2,760	2,720	2,765.5	50	21.8
	y_0	1,000	1,000	1,020	1,024.8	50	38.1

the original field is acquired by averaging points in a square such that only a small percentage of the total numbers of points are used for training the neural network. The number of neurons and the spread factor are chosen such that the 'normalized SSE' between low resolution of the actual field and the estimated field is kept below an acceptable threshold of 1. As a typical case, we assume a grid size of $n \times n = 20 \times 20$, spread factor of 30, with five neurons. The two-norm of error between actual and initial estimated field is 38.7 and error extrema are -144 and 204.

A similar scheme is used to approximate the complex field which is generated using CA discussed in Section 3.2. Since the field is very complex, more neurons are required for a good approximation. At a particular time, a low-resolution version of field is taken by considering a grid size of 20 × 20 and passed through RBF NN training for 20 neurons and spread factor of 40. The training using the hybrid algorithm only takes 2–3 s for 60 neurons neural network. Hence, the training time is much smaller than the speed of field evolution.

The plots shown in Fig. 12 are the two-norm of relative error of all the points in the actual field and in the neural network estimated field. The NN is trained on lower resolutions of the actual field with grid sizes of $n \times n = 5 \times 5$, 10×10 and 20×20. In Fig. 12a 5×5 size grid sampling is considered, therefore the error is smaller compared to Fig. 12b where we use a 10×10 size grid. An increase in the number of neurons decreases the error, but after a while, the error does not reduce any further.

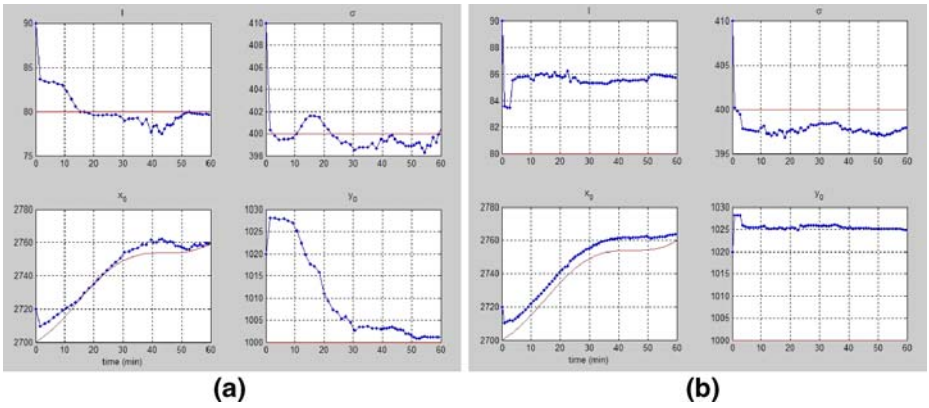

Fig. 10 Actual (red) and estimated (blue) fire field parameters I, σ, x_0 and y_0 versus time when sampling operation is performed until 60 min using greedy approach (**a**) and Raster scanning (**b**)

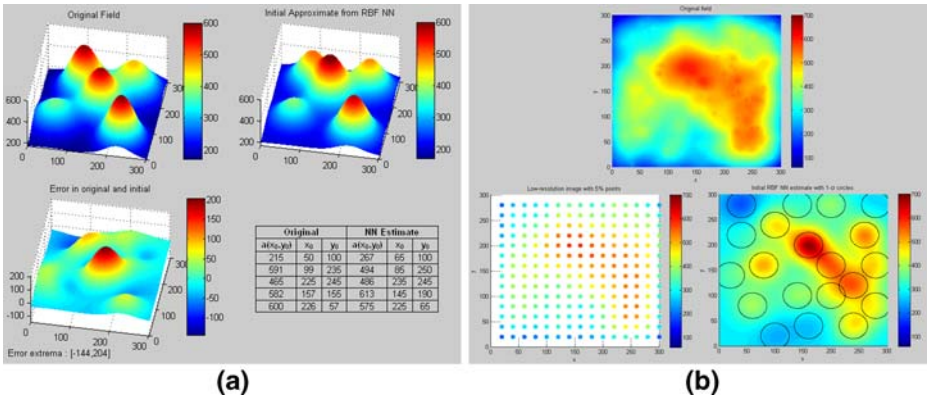

Fig. 11 (**a**) Sum-of-five Gaussians fire field approximation using 5 RBF neurons, (**b**) Complex field approximation using 20 neurons and a grid size of 20 × 20

For a spread factor of 40 and 60, the error stays the same even if more than 40 neurons are considered. Figure 12c illustrates the obvious fact that taking smaller size grid (indicating a higher resolution) increases the accuracy of initial estimate with the same number of neurons. As the number of neurons increases the initial

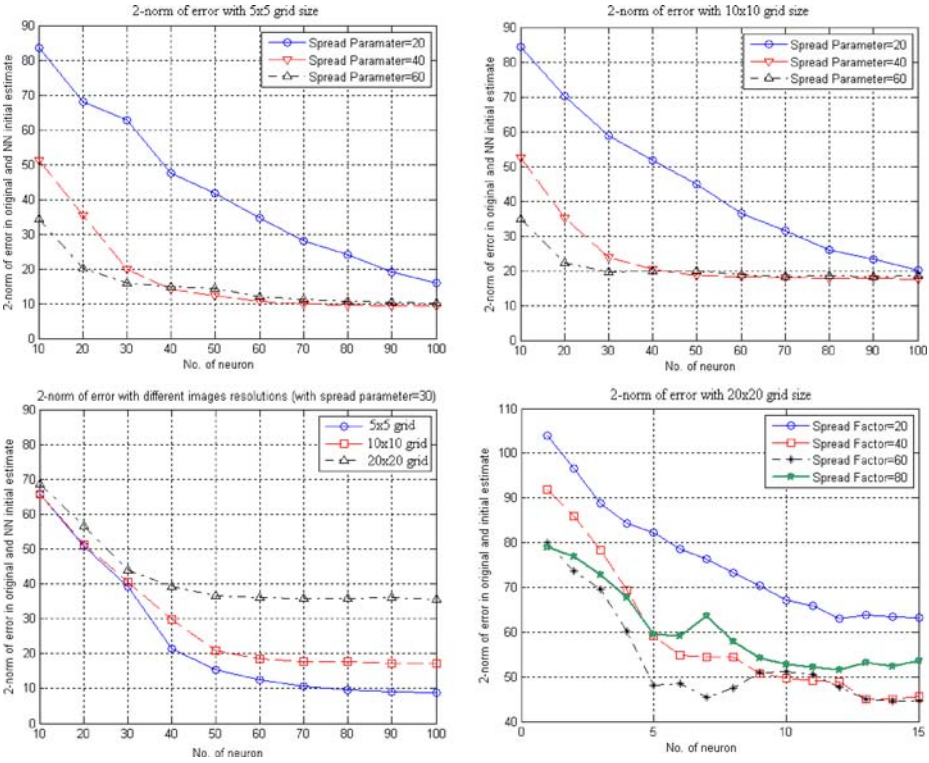

Fig. 12 Effect of number of neurons, spread factor and number of training points on the error in estimate

estimate gets better. This is valid until the neural network becomes over-trained. Figure 12d shows the error in approximating a Sum-of-Five-Gaussians field with RBF NNs with different number of neurons, when a 20×20 size grid and different spread factors are considered. An increase in the spread factor decreases the error as the number of neurons increase, but leads to saturation as shown in Fig. 12d where the error for spread factor of 80 is higher compared to a spread factor of 60. After the initial training, sampling simulations are performed to improve the estimate the 21 parameters. Our assumptions for uncertainties were:

$$P_{b0} = 200,\ P_{a0} = 50,\ P_{\sigma 0} = 10^{-8},\ P_{x00} = 4,\ P_{y00} = 4$$
$$Q = 0,\ R = 1 \tag{27}$$

A comparison of GAS and raster scanning is performed. The sampling area is divided into square grids and neighborhoods of different horizons. For GAS, we use a grid size of $n = 5$, $p = 5$ and horizon size of five square grids. Furthermore, the horizon size for GAS is kept such that it includes surrounding Gaussians. The result is that the next sample selected is in the vicinity of the neighboring Gaussian

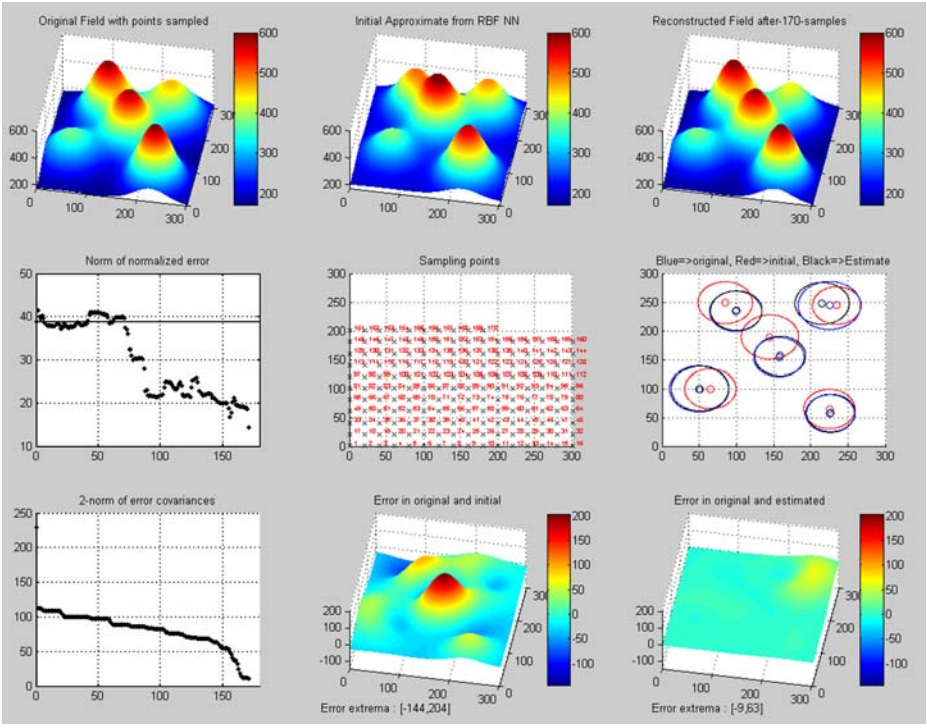

Fig. 13 Raster Scan simulation results shows that it takes 170 samples to achieve the norm of error in the original and estimated field less than 15, and the 2-norm of error covariance reduces from 229.5 to 10.72. A comparison of initial and final errors in shown in (**h**) and (**i**). As shown in (**f**), black circles start from their initial position (which is same as the red one), and chase the blue circles as the estimate becomes more accurate

whose parameters have high error covariance. This does not remove the possibility of the GAS algorithm running into local extrema in some special cases of time-varying field distributions. Based on experimental experience with hundreds of simulations, we have not observed this kind of effect; however, like most local gradient search methods, local extrema situations might be encountered. An example would be when the error covariance of parameters representing two Gaussians as well as the actual values of parameters is close enough. In that case, GAS might keep on directing the robot to sample back and forth in the vicinity of those two Gaussians and not come out of that loop. We further impose that unique locations are only sampled once, preventing local minima situations.

The simulation stops when the two-norm of error in actual and estimated field reduces below 15. It is shown in Figs. 13 and 14d that at the start of sampling 'Black' circles coincides with the 'Red' circles but start chasing the 'Blue' circles as the sampling continues. Table 2 indicates the Greedy AS is better than raster scan in terms of distance (time) as well as number of samples. Also, it can be seen from Figs. 13 and 14 that the estimation error and the norm of the error covariance decrease faster in case of GAS.

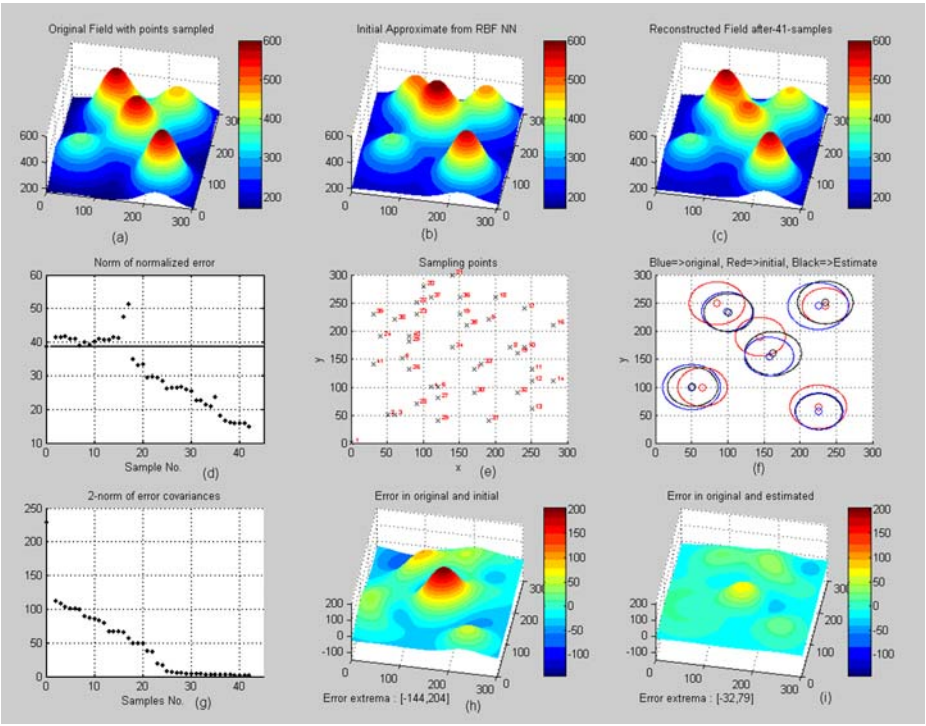

Fig. 14 GAS simulation results shows that it takes 41 samples to achieve the norm of error in the original and estimated field less than 15, and the 2-norm of error covariance reduces from 229.5 to 2.04. A comparison of initial and final errors in shown in (**h**) and (**i**). As shown in (**f**), black circles start from their initial position (which is same as the red one), and chase the blue circles as the estimate becomes more accurate

Table 2 Comparison of raster scan and greedy AS

	Greedy AS	Raster scan
Distance	2,175	3,400
No. of samples	41	170
Initial 2-norm of error in actual and estimated field	38.7	38.7
Final 2-norm of error in actual and estimated field	14.97	14.26
Initial 2-norm of error covariance	229.5	229.5
Final 2-norm of error covariance	2.04	10.72

7.3 Complex RBF Time-varying Field

We now increase the complexity of the fire field model by considering a slow time varying complex field generated using a CA. As the algorithm uses nonlinear Kalman filter, the observability of the parameters depends on the initial conditions. The initial error covariance is selected depending on the error in actual field and the initial estimated field, which in turn depends on the percentage of data from the actual

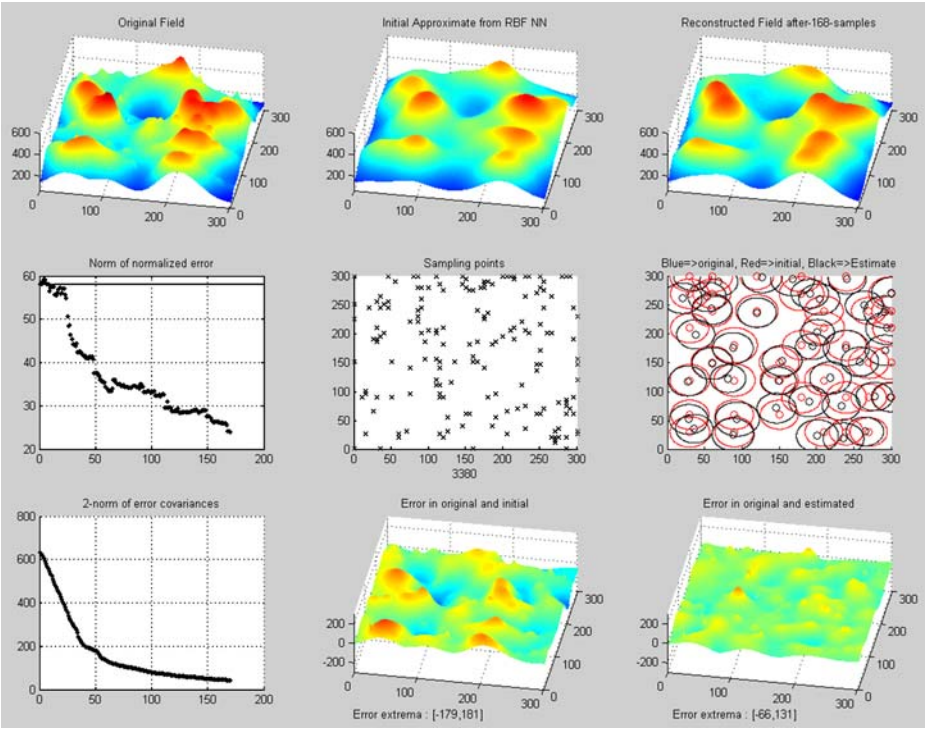

Fig. 15 GAS simulation showing (**a**) actual field generated using CA, (**b**) initial approximate with 40 neuron RBF-NN and spread factor of 30 when grid size of $n = 30$ is used for low-resolution sampling, (**c**) reconstructed field after 168 samples with GAS heuristic sampling approach when grid size of $p = 5$ is used for high-resolution sampling, (**d**) sum-of-square Error (SSE) in actual and estimated field which is shown to drop down faster compared raster scanning, (**e**) sampled points, (**f**) red and black circles indicate initial and estimated Gaussian locations respectively, (**g**) two-norm of error covariance of parameter estimates which is shown to drop down faster compared raster scanning, (**h**) error in actual and initial estimate, (**i**) error in actual and final estimate after 168 samples

Table 3 Comparison of raster scan and greedy AS

	Greedy AS	Raster scan
Distance	3,380	19,020
No. of samples	168	951
Initial 2-norm of error in actual and estimated field	58.07	58.07
Final 2-norm of error in actual and estimated field	23.95	27.49
Initial 2-norm of error covariance	632.5	632.5
Final 2-norm of error covariance	43.23	33.62

field, which is used for training the neural network, number of neurons and spread parameter.

The field is defined in a $m \times m = 300 \times 300$ area and an average of values in a $n \times n = 30 \times 30$ grid is used for training a NN with 40 neurons and a spread parameter of 30. We also assume the following noise and initial error covariances:

$$\begin{aligned} P_{b0} &= 100,\ P_{a0} = 5,\ P_{\sigma 0} = 10^{-7},\ P_{x00} = 1,\ P_{y00} = 1, \\ Q_{b0} &= 0.02\ Q_{a0} = 0.02,\ Q_{\sigma 0} = 0,\ Q_{x00} = 0,\ Q_{y00} = 0, \\ R &= 1 \end{aligned} \tag{28}$$

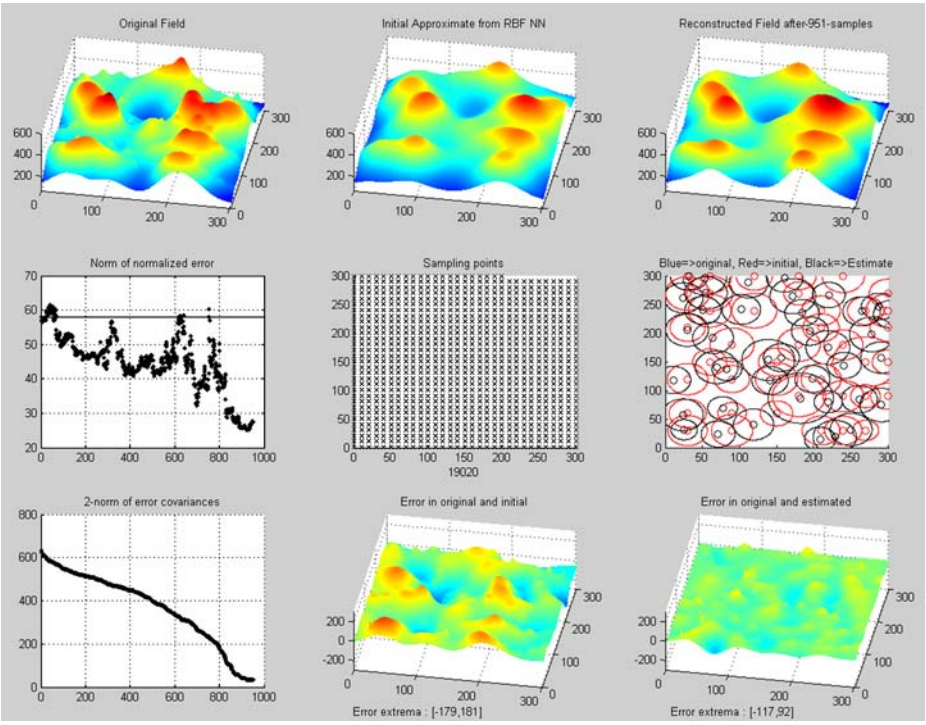

Fig. 16 Raster scan simulation showing (**a**) actual field generated using CA, (**b**) initial approximate with 40 neuron RBF-NN and spread factor of 30 when grid size of $n = 30$ is used for low-resolution sampling, (**c**) reconstructed field after 951 samples with raster scanning when grid size of $p = 10$ is used for high-resolution sampling, (**d**) sum-of-square Error (SSE) in actual and estimated field, (**e**) sampled points, (**f**) red and black circles indicate initial and estimated Gaussian locations respectively, (**g**) 2-norm of error covariance of parameter estimates, (**h**) error in actual and initial estimate, (**i**) error in actual and final estimate after 951 samples

Figure 16 shows the raster scanning simulation results when sampling in performed row-by-row in a grid size of $p \times p = 10 \times 10$. Figure 15 shows the GAS simulation results with grid size of $p \times p = 5 \times 5$. Grid size is an important parameter. A very large grid size will not reduce the error significantly even if the whole area is scanned because thorough sampling is required in high-variance areas. As the robots start sampling with given initial estimates and uncertainties, the uncertainty of the parameters does not decrease until the robot reaches the area where those parameters have significant influence. In other words, the uncertainty of the Gaussian is most reduced when sampling is performed within few a few σ from its center.

A comparison of GAS and raster scanning is shown in Table 3. It is observed that since raster scan performs a row-by-row scanning, it takes a longer time and more samples. The simulation stops when two-norm of error in actual and estimated field reduces below a threshold. It can be seen from Figs. 15 and 16 that the sum of square error (SSE) in actual and estimated field as well as the two-norm of state error covariances decreases faster in case of GAS.

8 Experimental Testbed with Projection System and Robots

In order to experimentally validate our algorithms, we have set up an in-door testbed. The hardware includes a camera–projector system and the mobile wireless sensor nodes (ARRI-Bots) [31, 32]. These are inexpensive units built in our lab. ARRI-Bots consists of Javelin stamp CPU, Cricket® processor and radio module, wheel encoders for dead-reckoning localization, ultrasonic rangefinders for obstacle detection and a color sensor. We run the EKF-based adaptive sampling algorithm from a central PC, from which we direct the robots to sample at appropriate locations and estimate the field parameters. The PC also generates the time-varying fire field distribution and projects it on the lab floor where the robots are sampling color

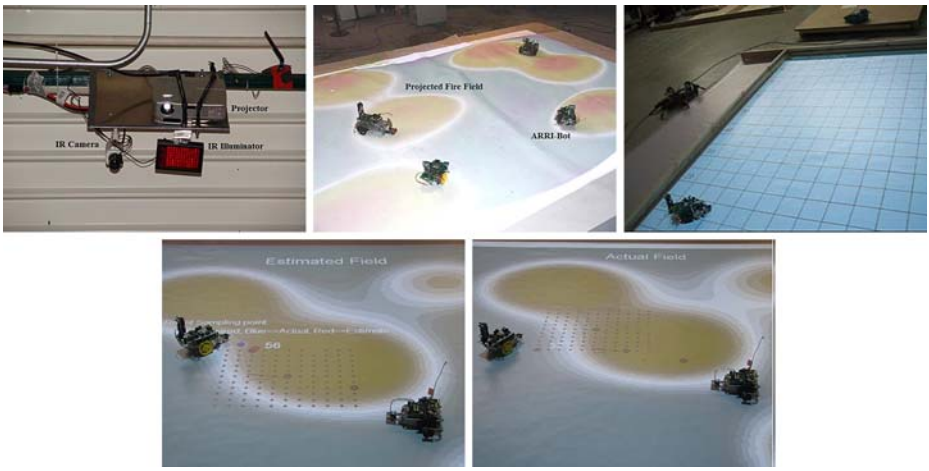

Fig. 17 Testbed with simulated fire field projected on the floor from a projector. ARRI-Bots are shown sampling at various locations for estimating field parameters. An overhead IR camera is used to aid in localization and for validating the accuracy of estimated location

as shown in Fig. 17. The area of projection is approximately 15 ft in diagonal with projector mounted 20 ft high. The overhead camera is used as "GPS" in conjunction with MATLAB's Image Acquisition and Image Processing toolboxes. An initial estimate of the parameters is obtained using a low-resolution version of the field image as explained in previous sections. Multiple wireless robots perform sampling mission to correct the field parameter estimates.

8.1 Experimental Results for Adaptive Sampling with Two Robots

Experimental results are shown in Fig. 18 for a field projected in an area of 124 × 90 square inches. Figure 18a shows the field that is generated using CA. A low-resolution grid size with $n = 20$ gives 27 (3×3) samples for training the neural network. We use 20 neurons and a spread factor of 25 to approximate the field with 80 parameters (20×4). Two robots sample the field in parallel using GAS algorithm with grid size $p = 5$ and horizon size 3.

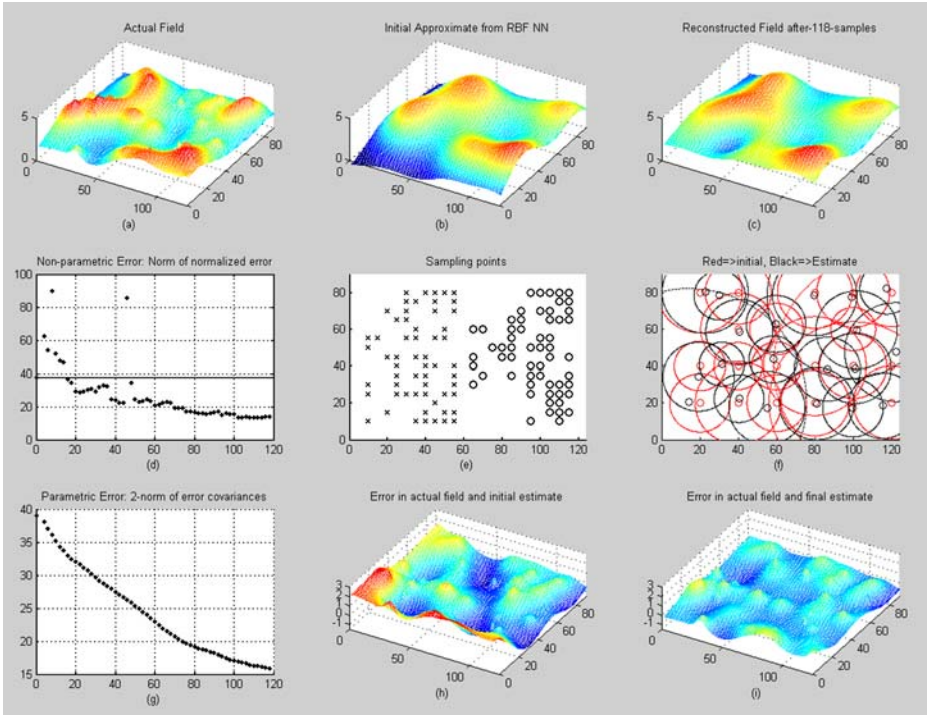

Fig. 18 Experimental results for estimation of a complex field represented by 20 neuron RBF showing (**a**) actual field generated using CA is projected in an area of 124 × 90 square inches on the floor where 2 robots sample using GAS algorithm, (**b**) initial approximate with 20 neuron RBF-NN and spread factor of 25 with grid size of $n = 20$ used for low-resolution sampling, (**c**) reconstructed field after 118 samples using GAS with grid size of $p = 5$ and horizon size = 3 used for high-resolution sampling, (**d**) sum-of-square error (SSE) in actual and estimated field, (**e**) locations sampled by two robots represented by 'x' and 'o' symbols, (**f**) red and black circles indicate initial and estimated Gaussian locations respectively, (**g**) two-norm of error covariance of parameter estimates, (**h**) error in actual and initial estimate, (**i**) error in actual and final estimate after 118 samples

Figure 18b and c respectively shows the initial field and final estimated field after 118 samples. Figure 18e indicates the locations by 'x' and 'o' symbols where the two robots took samples. As shown in Fig. 18 and g, the parametric error drops down from 37.6 to 13.91, and the non-parametric error drops from 39.05 to 15.86 by taking 118 samples. This final non-parametric error is close to what we would get if we sample data from actual field assuming a grid size of 5 (which uses 446 samples) to train the neural network.

The assumptions for uncertainties were:

$$P_{b0} = 5,\ P_{a0} = 5,\ P_{\sigma 0} = 10^{-4},\ P_{x00} = 5,\ P_{y00} = 5$$
$$R = 0.01 \tag{29}$$

The use of two robots instead of one for sampling also reduces the time for reconstruction from 6.7 to 2.6 min (which is less than half). This can be understood intuitively because not only the number of samples per robot reduces, but also navigation time reduces in a smaller sampling area.

8.2 Distributed Multi-Robot Sampling

In a practical forest fire tracking scenario, a fire field will be represented by many parameters, and plenty of computations will be required to run the Kalman filter. The field used in simulations of Section 7.3 is represented by 120 parameters; therefore, 120×120 matrix computations are required to select candidate sampling locations. Therefore, it will quickly become unfeasible for individual robots to run the EKF-AS algorithm and share large covariance matrices wirelessly.

Clearly, distributing the computational load and the coverage area among robots is a better choice. Each robot will run the AS algorithm and generate new locations within the vicinity of its current position. The robots will take the measurements and calculate only partial estimates of the field. After every few samples, the robots will communicate and share their information. The parameter estimate and the error covariance are the two terms each robot will transmit. Hence, each robot will assimilate the received information using for instance a distributed EKF scheme similar to [35]. Using this scheme, the sum of computations performed by all the robots will be more than the processing by just one robot doing sampling. But the speed of convergence and reduction in complexity that will be gained by using multiple robots will be significant. With a single robot, total field estimation time includes the time necessary for navigation, sensing and computations of estimate (as there is no communication). With multiple robots, the field estimation time includes the time taken for sensing, computation, communication, and final fusion to recover the field. The speed of convergence will increase using multiple robots simply because of sampling in parallel as the navigation time reduces significantly compared to modest increases in computation, communication and fusion.

This approach works well if reliable communication among robots is accomplished. If only local communication is available, a distributed Kalman filter can be implemented using consensus filters where each robot communicates with its neighbors as in [29]. Additional improvements can be obtained by ignoring the correlation among parameters that are far in space in order to reduce the computational overhead. Future experiments will be conducted to confirm the performance of a distributed sampling algorithm.

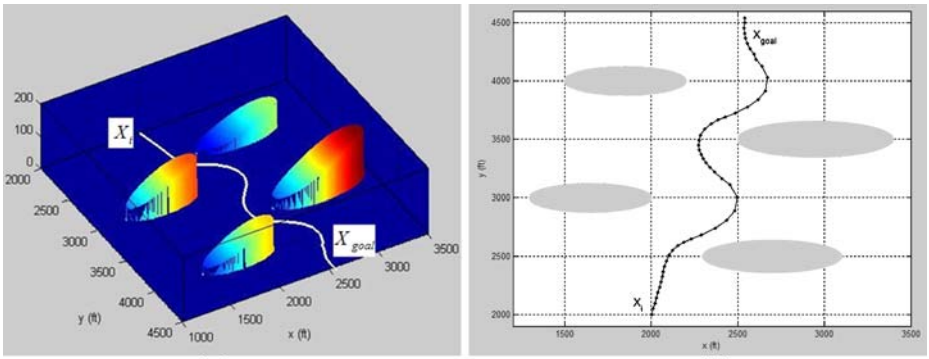

Fig. 19 Estimated fire ellipses and dynamically generated path using potential fields for the human firefighter to go from X_i to rescue location X_{goal}

9 Potential Fields for Safe Trajectory Generation

Simulations are performed to generate fire-safe paths through the estimated field, as shown in Fig. 19. We have assumed that there are four fire ellipses and there are multiple robots sampling in their designated areas. Every robot runs a separate EKF-based AS algorithm to estimate the parameters of its local fire field. Fire field data are then aggregated in a central processing location, which is also responsible for on-line fire-safe trajectory generation. We dynamically update the trajectory from X_i to X_{goal} every time the field parameters estimate updates. In a practical implementation scenario, a human firefighter can carry a wireless device receiving estimates from the robots in order to generate a collision-free path around fire obstacles toward the goals using Eqs. 23 and 24. Assuming the human crew is at location $X_i = (2000, 2000)$ and needs to go to rescue location $X_{\text{goal}} = (2500, 4500)$, the path is divided into 50 segments and repulsive forces from each of these virtual obstacles, and attractive force toward the goal is calculated. The numerical coefficients used in the simulation are: $\xi = 1$, $\lambda = 10^6$, $\delta = 0.01$. The trajectory is updated using this suitable δ and net force $\vec{F}_p$ value using Eq. 25.

10 Conclusion and Future Work

This paper presents a multi-scale approach for mapping forest fires using an EKF-based adaptive sampling algorithm. Two types of parametric descriptions are introduced for modelling of the forest fire spread. The first one assumes elliptically constrained RBF distributions, while a second one is generated using Cellular Automata (CA). The proposed sampling algorithm (EKF-NN-GAS) uses a multi-scale, multi-rate approach, achieved by taking two types of measurements, local and global. Low-resolution (high-field of view) data are approximated with a RBF-NN trained using self-organized selection of centers, in order to obtain an initial parameter estimates. More Gaussians overlapping in high-variance areas will ultimately lead to thorough robotic sampling in those areas. This initial estimate, though clustered, is inaccurate due to low-resolution sampling and training errors. The field estimate is further refined by high-resolution (local) sampling via robots.

Simulation and experimental results show that the heuristic greedy approach performs much better than raster scanning in terms of time and number of samples because it looks for locations providing maximum information about the parameters. For a typical case considered in Section 7.3, simulation results show that the reconstruction time is about six times faster and requires six times less number of samples. Experimental results with two sampling robots show a further reduction in time by factor of more than 2. Finally, in order to navigate through the field, a potential field utilizing the estimated fire field is used to generate a safe-path trajectory for human crews.

Future work includes considering the uncertainty in localization and situations where combined EKF scheme can help in localization when GPS measurements are not available. We are also working on a distributed EKF scheme, which ultimately will reduce the computational complexity and communication among the robots. Finally, plans are also being made for implementation of the sampling algorithms using multi-scale robots equipped with thermal imaging equipment and topographic mapping.

References

1. Anderson, B., Moore, J.: Optimal Filtering. Prentice-Hall, Englewood Cliffs, NJ (1979)
2. Anderson, D.H., Catchpole, E.A., DeMestre, N.J., Parkes, T.: Modeling the spread of grass fires. J. Aust. Math. Soc. (Ser. B.) **23**, 451–466 (1982)
3. Cannell, C.J., Stilwell, D.J.: A comparison of two approaches for adaptive sampling of environmental processes using autonomous underwater vehicles. Oceans **2**, 1514–1521 (2005)
4. Christopoulos, V.N., Roumeliotis, S.: Adaptive sensing for instantaneous gas release parameter estimation. International Conference on Robotics and Automation, 2005. ICRA 2005. In: Proceedings of the 2005 IEEE, pp. 4450–4456. (2005) 18–22 Apr
5. Chuvieco, E. (ed.): Wildland Fire Danger Estimation and Mapping: The Role of Remote Sensing Data. World Scientific Publishing Company, New Jersey, USA (2004)
6. Creed, E.L., Glenn, S.M., Chant, R.: Adaptive sampling experiment at LEO-15. OCC 1998 Proceedings, Marine Technology Section. pp. 576–579 (1998) Nov
7. Elfes, A.: Using occupancy grids for mobile robot perception and navigation. Computer. **22**(6), 46–57 (1989)
8. Farrell, J.A., Shuo, P., Wei, L.: Chemical plume tracing via an autonomous underwater vehicle. IEEE J. Oceanic. Eng. **30**(2), 428–442 (2005)
9. Finney, M.A.: FARSITE: fire area simulator-model development and evaluation. Res. Pap. RMRS-RP-4. U.S. Department of Agriculture, Forest Service, Rocky Mountain Research Station, Ogden, UT, p. 47 (1998)
10. Fox, D., Burgard, W., Kruppa, H., Thrun, S.: A probabilistic approach to collaborative multi-robot localization. Auton Robots. **8**(3), 325–344 (2000), Special issue on Heterogeneous Multi-Robot Systems
11. Ge, S.S., Cui, Y.J.: Dynamic motion planning for mobile robots using potential field method. Int. J. Auton. Robots. **13**, 207–222 (2002)
12. Green, D.G.: Shapes of simulated fires in discrete fuels. Ecol. Mod. **20**, 21–32 (1983)
13. Green, D.G., Gill, A.M., Noble, I.R.: Fire shapes and the adequacy of fire-spread models. Ecol. Mod. **20**, 33–45 (1983)
14. Haykin, S.: Neural Networks: A Comprehensive Foundation, 2nd. Prentice Hall, USA (1998)
15. Hombal, V., Sanderson, A., Blidberg, R.: A non-parametric iterative algorithm for adaptive sampling and robotic vehicle path planning. International Conference on Intelligent Robots and Systems, 2006 IEEE/RSJ, pp. 217–222. (2006) Oct
16. Howard, A., Mataric, M.J., Sukhatme, G.S.: Mobile sensor network deployment using potential fields: a distributed, scalable solution to the area coverage problem. In: Proc. of 6th International Symposium on Distributed Autonomous Robotic Systems. Fukuoka, Japan, pp. 299–308 (2002)
17. Jatmiko, W., Sekiyama, K., Fukuda, T.: A mobile robots PSO-based for odor source localization in dynamic advection-diffusion environment. In: International Conference on Intelligent Robots and Systems, 2006, IEEE/RSJ. pp. 4527–4532 (2006) Oct

18. Johnson, E.A., Miyanishi, K. (ed.): Forest Fires-Behavior and Ecological Effects. Academic, San Diego (2001)
19. Karafyllidis, I., Thanailakis, A.: A model for predicting forest fire spreading using cellular automata. Ecol. Mod. **99**, 87–97 (1997)
20. Khatib, O.: Real-time obstacle avoidance for manipulators and mobile robots. In: Proc. IEEE, International Conference on Robotics and Automation, pp. 500–505. (1985) 25–28 Mar
21. Krogh, B.H.: A generalized potential field approach to obstacle avoidance control. In: Proc. of International Robotics Research Conference. pp. 1150–1156 (1984) Aug
22. Latombe, J.: Robot Motion Planning. Academic, Boston (1991)
23. Lewis, F.L., Xie, L., Popa, D.O.: Optimal and Robust Estimation: With an Introduction to Stochastic Control Theory. CRC, Florida, USA (2007)
24. Li, X., Yeh, A.G..: Neural-network-based cellular-automata for simulating multiple land use changes using GIS. Int. J. Geogr. Inf. Sci. **16**(4), 323–344 (2002)
25. Lippmann, R.P.: Pattern classification using neural networks. Commun. Mag, IEEE. **27**(11), 47–50, 59–64 (1989) Nov
26. Low, K.H., Gordon, G.J., Dolan, J.M., Khosla, P.: Adaptive Sampling for Multi-Robot Wide-Area Exploration. In: 2007 IEEE International Conference on Robotics and Automation. pp. 755–760, (2007) 10–14 Apr
27. Mandel, J., Darema, F. (ed.): Dynamic Data Driven Wildfire Modeling. Dynamic Data Driven Applications Systems. Academic, New York (2004)
28. Muzy, A., Innocenti, E., Aiello, A., Santucci, J., Wainer, G.: Specification of discrete event models for fire spreading. Simulation **81**(2), 103–117 (2005)
29. Olfati-Saber, R.: Distributed Kalman filter with embedded consensus filters. In: 44th IEEE Conference Decision and Control, 2005 and 2005 European Control Conference. CDC-ECC '05 pp. 8179–8184, (2005) 12–15 Dec
30. Popa, D.O.: Optimal sampling using singular value decomposition of the parameter variance space. In: 2005. (IROS 2005). In: 2005 IEEE/RSJ International Conference on Intelligent Robots and Systems, pp. 3131–3136, (2005) 2–6 Aug
31. Popa, D.O., Mysorewala, M.F., Lewis, F.L.: EKF-based adaptive sampling with mobile robotic sensor nodes. In: International Conference on Intelligent Robots and Systems, 2006 IEEE/RSJ, pp. 2451–2456 (2006) Oct
32. Popa, D.O., Mysorewala, M.F., Lewis, F.L.: Deployment Algorithms and In-Door Experimental Vehicles for Studying Mobile Wireless Sensor Networks. To appear in ACIS International Journal of Sensor Networks (2009)
33. Popa, D.O., Stephanou, H.E., Helm, C., Sanderson, A.C.: Robotic deployment of sensor networks using potential fields. In: The Proc. of International Conference on Robotics and Automation (2004) April–May
34. Popa, D.O, et al.: Adaptive sampling algorithms for multiple autonomous underwater vehicles. In: Autonomous Underwater Vehicles, 2004 IEEE/OES, pp. 108–118 (2004) 17–18 June
35. Rao, B.S., Durrant-Whyte, H.F.: Fully decentralised algorithm for multisensor Kalman filtering. IEE Proc Part D. **138**(5), 413–420 (1991)
36. Rothermel, R.C.: How to predict the spread and intensity of forest and range fires. Gen. Tech. Rep. INT-143. U.S. Department of Agriculture, Forest Service, Intermountain Forest and Range Experiment Station, Ogden, UT, p. 161 (1983)
37. Roumeliotis, S.I., Bekey, G.A.: Distributed Multi-Robot Localization. Distributed Autonomous Robotic Systems 4. Springer Verlag, New York, pp. 179–188 (2000)
38. Russell, R.A., Bab-Hadiashar, A., Shepherd, R.L., Wallace, G.G.: A comparison of reactive robot chemotaxis algorithms. Robot. Auton. Syst. **45**(2), 83–97 (2003) 30 Nov
39. Scott, D.: Multivariate Density Estimation: Theory, Practice, and Visualization. Wiley, New York (1992)
40. Silverman, B.: Density Estimation for Statistics and Data Analysis. Chapman & Hall/CRC, USA (1986)
41. Singh, A. et al.: Multiscale sensing: a new paradigm for actuated sensing of high frequency dynamic phenomena. In: International Conference on Intelligent Robots and Systems, 2006 IEEE/RSJ, pp. 328–335 (2006) Oct
42. Trunfio, G.A.: Predicting Wildfire Spreading through a Hexagonal Cellular Automata Model. ACRI, pp. 385–394 (2004)
43. Wagner, V.: A simple fire growth model. Forestry Chron. **45**, 103–104 (1969)